Supplementary Information (SI) for Journal of Materials Chemistry A.

Supplementary Information for

Incorporating Unique B-N Motifs into Graphene for Efficient Photocatalytic CO_2 Reduction

Huizhong Ma,[a] Honglei Yuan,[a] Yulong Wang,[a] Wenxing Xu,[b] Hongzhang Wu,[c] Lingling Sun,[a] Yan Zhang,[a] Xuejian Sun,*[a] Jin Feng*[b]

[a]*School of Physics and Telecommunication Engineering, Zhoukou Normal University, Zhoukou 466001, China*

[b]*Key Laboratory of Life-Organic Analysis of Shandong Province, School of Chemistry and Chemical Engineering, Qufu Normal University, Qufu 273100, China*

[c]*Henan Key Laboratory of Intelligent Biomaterials and Medical Applications, International Joint Research Laboratory for Biomedical Nanomaterials of Henan, Zhoukou Normal University, Zhoukou 466001, China*

**E-mail Addresses: 1589001511@qq.com (X. Sun), fengjinzuibang@163.com (J. Feng).*

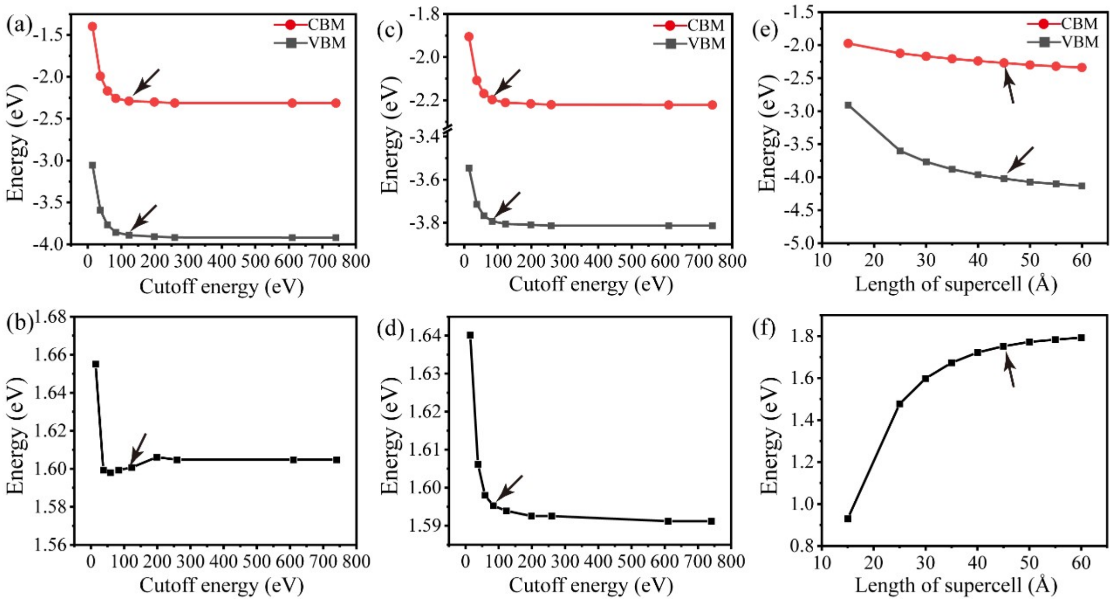

Figure S1. Convergence tests of parameters in GW calculations for 66Gr-6BN. (a) and (b): Evolution of the valence band maximum (VBM), conduction band minimum (CBM) and bandgap at the Γ point with the cutoff energy ($E_{(cut)}$) for the band summation over unoccupied orbitals in the self-energy evaluation. In this test, the $E_{(cut)}$ for electronic screening is fixed at 58.5 eV. (c) and (d): Evolution of the VBM, CBM and bandgap at the Γ point with the cutoff energy for the band summation in the electronic screening evaluation. In this test, the $E_{(cut)}$ for self-energy evaluation is fixed at 58.5 eV. In (a)–(d), the energy zero is set at the CBM, and the supercell length along the normal direction of 66Gr-6BN is set to 30 Å. (e) and (f): Evolution of the VBM, CBM and bandgap at the Γ point with the supercell length along the normal direction of 66Gr-6BN. In this test, the $E_{(cut)}$ for both self-energy and electronic screening is fixed at 58.5 eV. The actually adopted parameters are marked with an arrow in each panel.

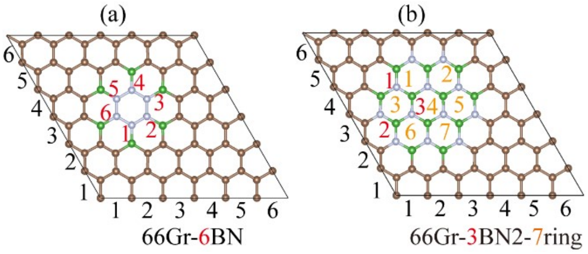

Figure S2. Nomenclature of B–N-embedded graphene structures. Schematic illustrations explaining the naming convention for (a) 66Gr-6BN and (b) 66Gr-3BN2-7ring, where "66Gr" denotes a 6×6×1 graphene supercell and the subsequent suffix specifies the type and configuration of incorporated B–N motifs.

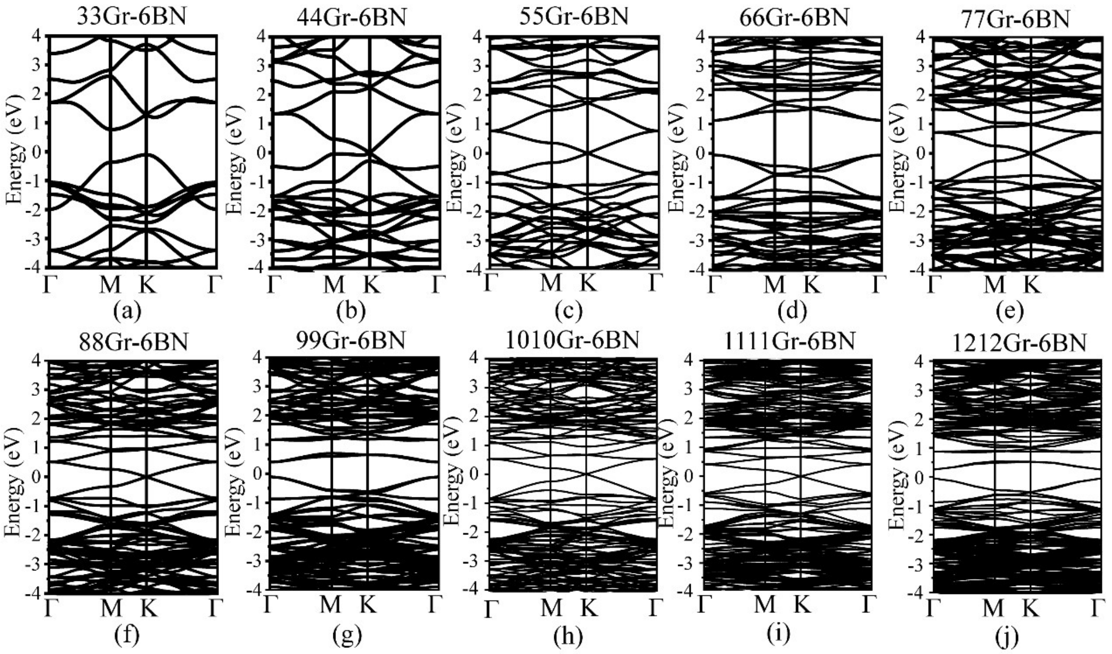

Figure S3. Band structures of graphene supercells containing six B–N bonds, computed using the PBE functional. The corresponding graphene supercell sizes are (a) 3×3×1, (b) 4×4×1, (c) 5×5×1, (d) 6×6×1, (e) 7×7×1, (f) 8×8×1, (g) 9×9×1, (h) 10×10×1, (i) 11×11×1, and (j) 12×12×1.

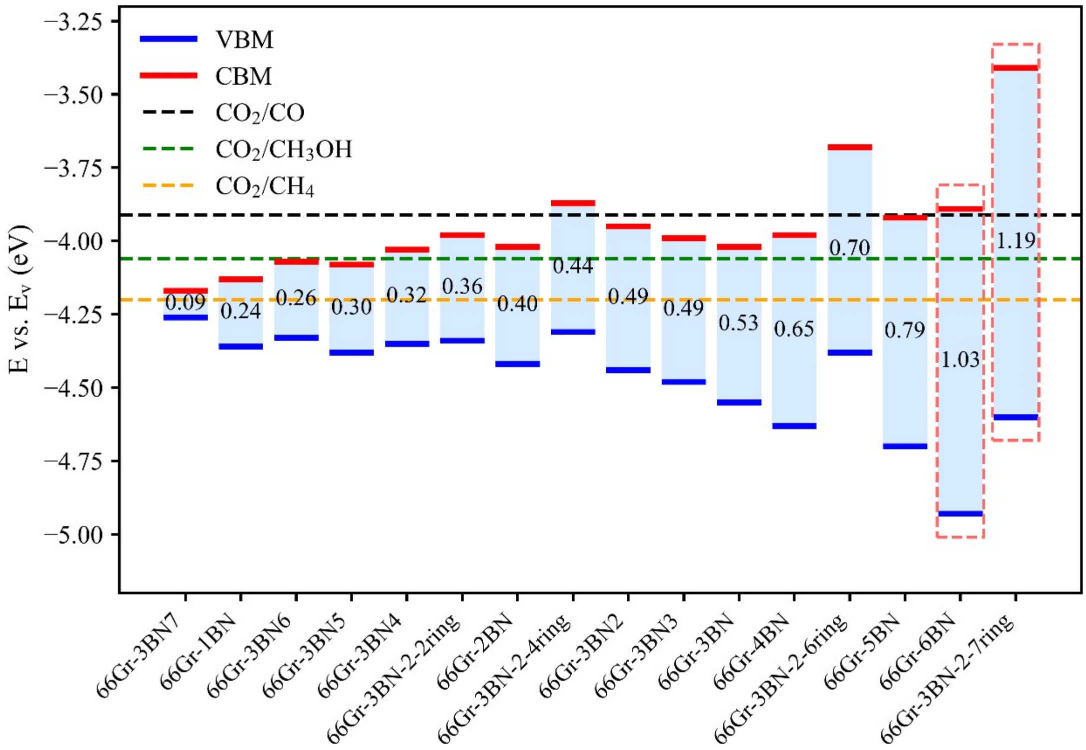

Figure S4. PBE band edges of the 16 screened configurations in Fig. 1a, c, and d, arranged in order of increasing bandgap and referenced to vacuum. Shaded regions indicate the PBE bandgaps. Dashed lines mark the CO_2/CO, CO_2/CH_3OH, and CO_2/CH_4 reduction potentials at pH 7. Red boxes mark the two structures retained for GW-BSE study.

Table S1. Measured bond length ranges for the five distinct bond types (C–C, C–B, N–N, C–N, and N–B) identified in 66Gr-6BN and 66Gr-3BN2-7ring.

	66Gr-6BN	66Gr-3BN2-7ring
C-C	1.38-1.43 Å	1.40-1.44 Å
C-B	1.49 Å	1.49 Å
N-N	1.37 Å	–
C-N	–	1.39 Å
N-B	1.45 Å	1.41-1.44 Å

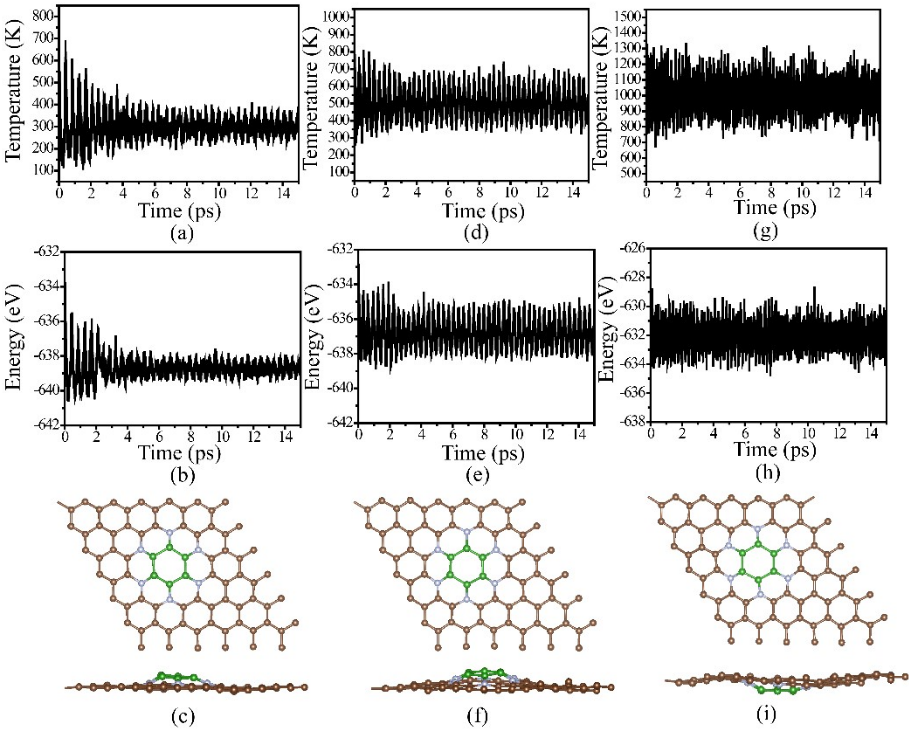

Figure S5. AIMD simulation results for 66Gr-6BN. (a, d, g) Temperature evolution, (b, e, h) total energy fluctuation, and (c, f, i) final structural configurations (top and side views) after 15 ps simulation at 298 K (a–c), 500 K (d–f), and 1000 K (g–i).

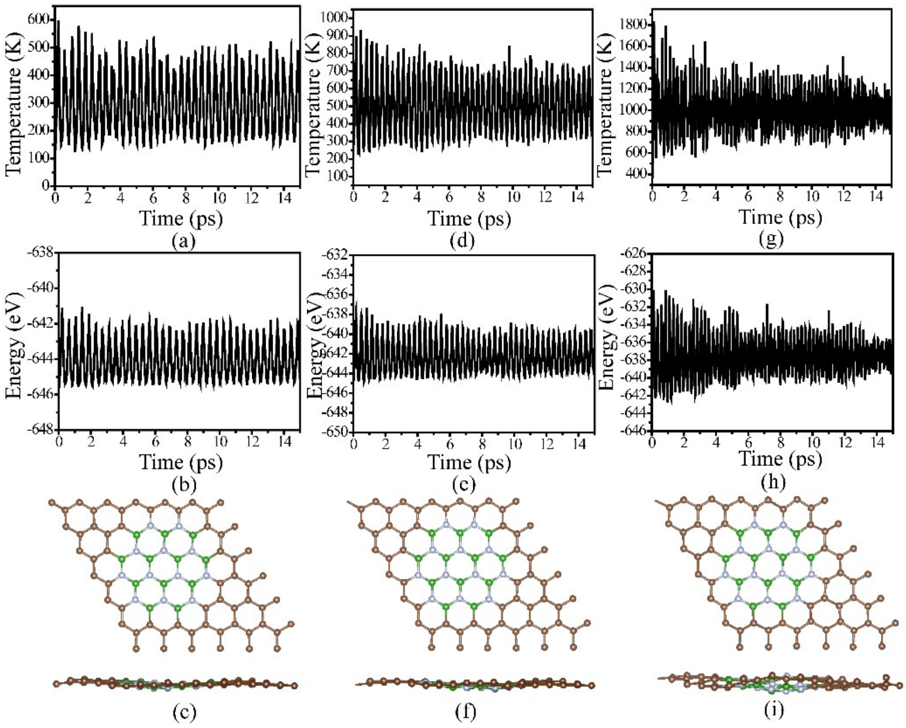

Figure S6. AIMD simulation results for 66Gr-3BN2-7ring. (a, d, g) Temperature evolution, (b, e, h) total energy fluctuation, and (c, f, i) final structural configurations (top and side views) after 15 ps simulation at 298 K (a–c), 500 K (d–f), and 1000 K (g–i).

Table S2. Total energy fluctuations of 66Gr-6BN and 66Gr-3BN2-7ring during 15 ps AIMD simulations at different temperatures. The energy fluctuation is defined as the difference between the maximum and minimum total energies observed during the simulation trajectory.

	298 K	500 K	1000 K
66Gr-6BN	7.89 eV	6.19 eV	6.17 eV
66Gr-3BN2-7ring	5.65 eV	9.40 eV	16.63 eV

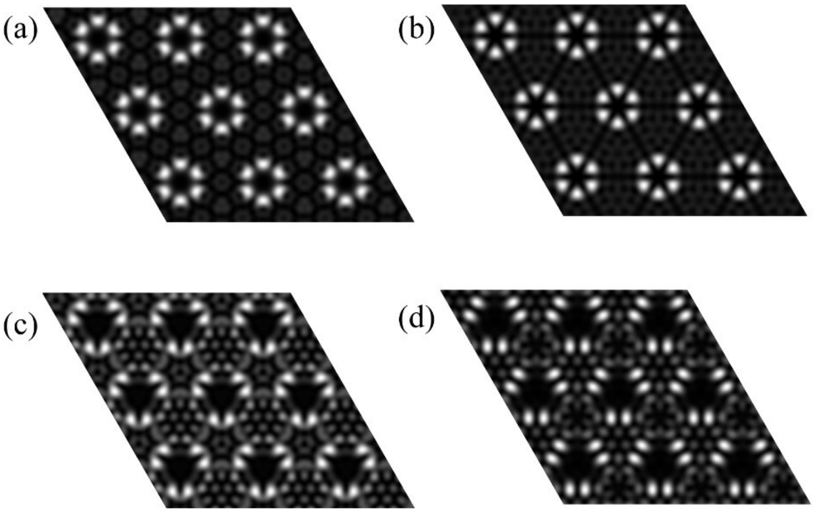

Figure S7. Simulated constant-current scanning tunneling microscope (STM) images of (a, b) 66Gr-6BN and (c, d) 66Gr-3BN2-7ring under filled-state (a, c) and empty-state (b, d) imaging.

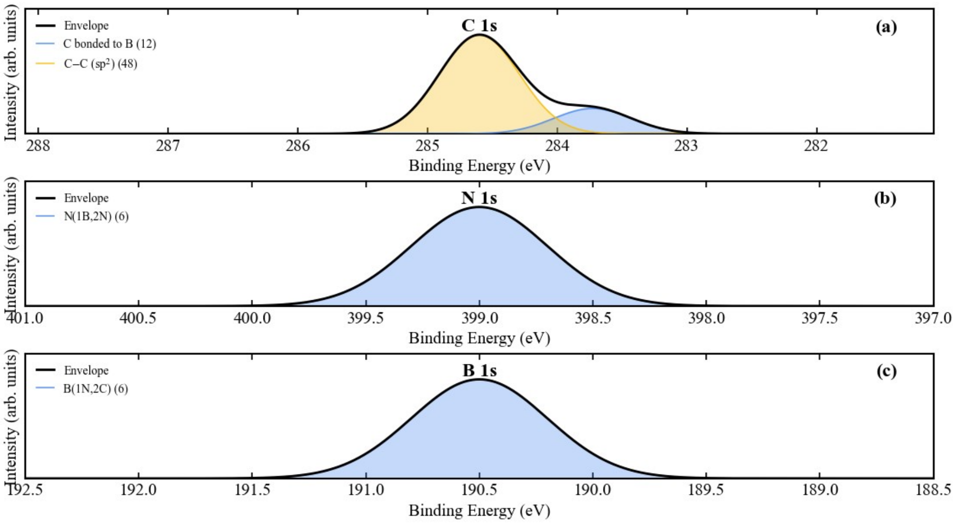

Figure S8. Simulated (a) C 1s, (b) N 1s, and (c) B 1s core-level X-ray photoelectron spectroscopy (XPS) spectra of 66Gr-6BN.

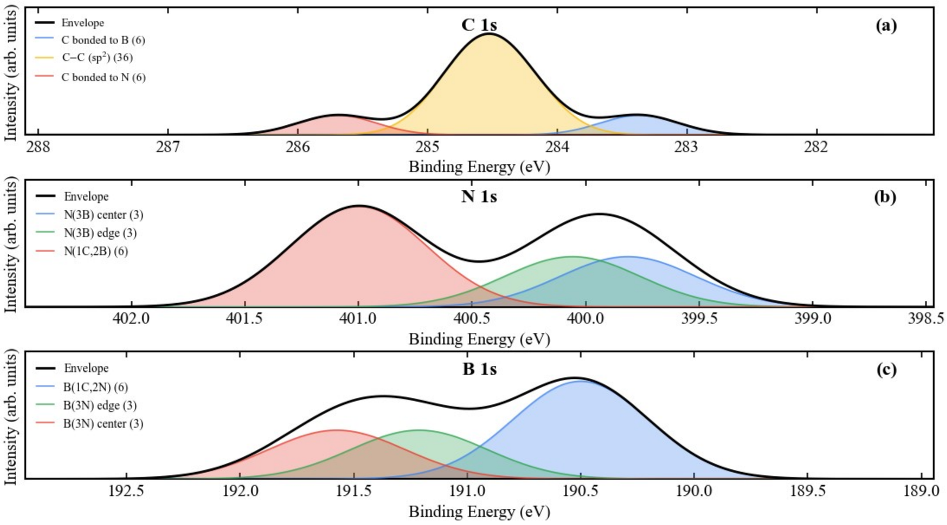

Figure S9. Simulated (a) C 1s, (b) N 1s, and (c) B 1s core-level X-ray photoelectron spectroscopy (XPS) spectra of 66Gr-3BN2-7ring.

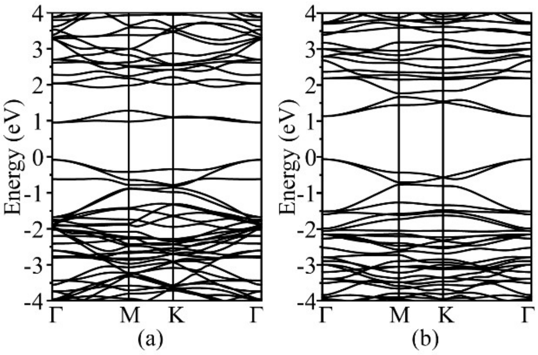

Figure S10. DFT-PBE band structures. Electronic band structures calculated using the PBE functional for (a) 66Gr-6BN and (b) 66Gr-3BN2-7ring, showing the characteristic direct bandgap at the Γ point for both structures. The Fermi level is set at 0 eV in both band structures.

Table S3. Exciton binding energy (E_b) and apparent quantum yield (AQY) of representative photocatalysts for CO_2 reduction,[1, 2] together with the predicted values for 66Gr-6BN and 66Gr-3BN2-7ring in this work.

Photocatalyst	E_b (eV)	AQY (%)	Main product	Light source	Ref.
g-C_3N_4 (urea precursor)	~3.0	0.18	CH_3OH	λ = 420 nm	75
P,C-codoped g-C_3N_4	reduced vs g-C_3N_4	0.42	CH_4	λ = 420 nm	76
TiO_2 (microchannel reactor)	~0.2	0.0301	CO	UV-Vis	S1
TiO_2-in-MIL-101-Cr-NO_2	N/A	11.3	CO + CH_4	λ = 350 nm	78
Fibrous phosphorene	N/A	1.36	CO	λ = 620 nm	S2
66Gr-6BN (this work)	0.063 (β)	N/A (predicted)	CO, CH_3OH, CH_4	Visible	N/A
66Gr-3BN2-7ring (this work)	0.059 (χ)	N/A (predicted)	CO, CH_3OH, CH_4	Visible	N/A

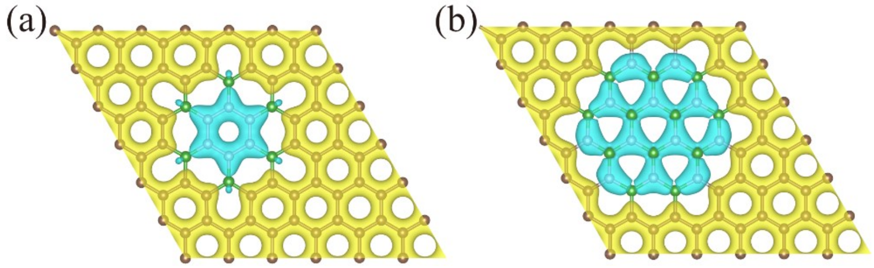

Figure S11. Differential charge density of (a) 66Gr-6BN and (b) 66Gr-3BN2-7ring. Yellow (light blue) isosurfaces represent electron accumulation (depletion).

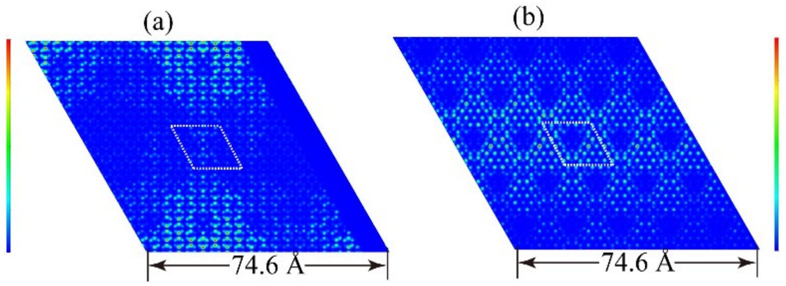

Figure S12. Spatial distributions of photoexcited electrons for (a) the β state, the state possessing the largest oscillator strength in 66Gr-6BN, and (b) the χ state, the state possessing the largest oscillator strength in 66Gr-3BN2-7ring. The corresponding hole is confined to the central unit cell, marked by a white dashed parallelogram.

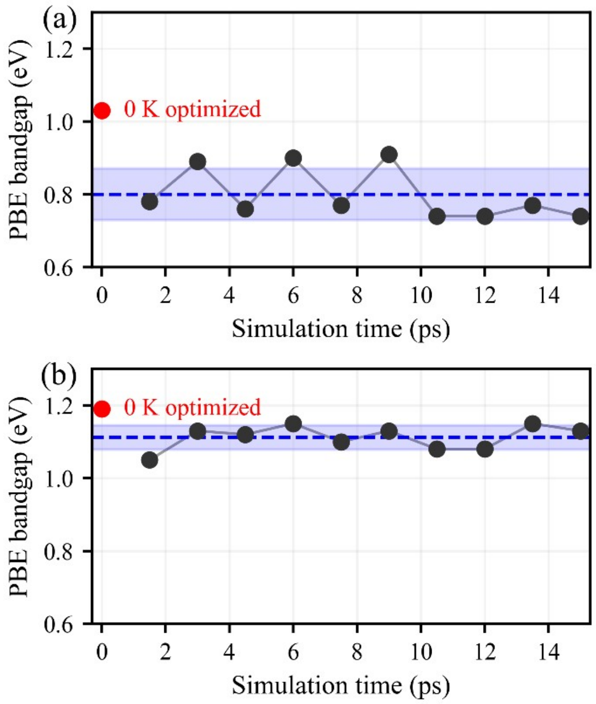

Figure S13. PBE bandgap evolution during 15 ps AIMD simulations at 298 K for (a) 66Gr-6BN and (b) 66Gr-3BN2-7ring. The red point indicates the 0 K optimized value; the dashed line and shaded region show the mean ± one standard deviation.

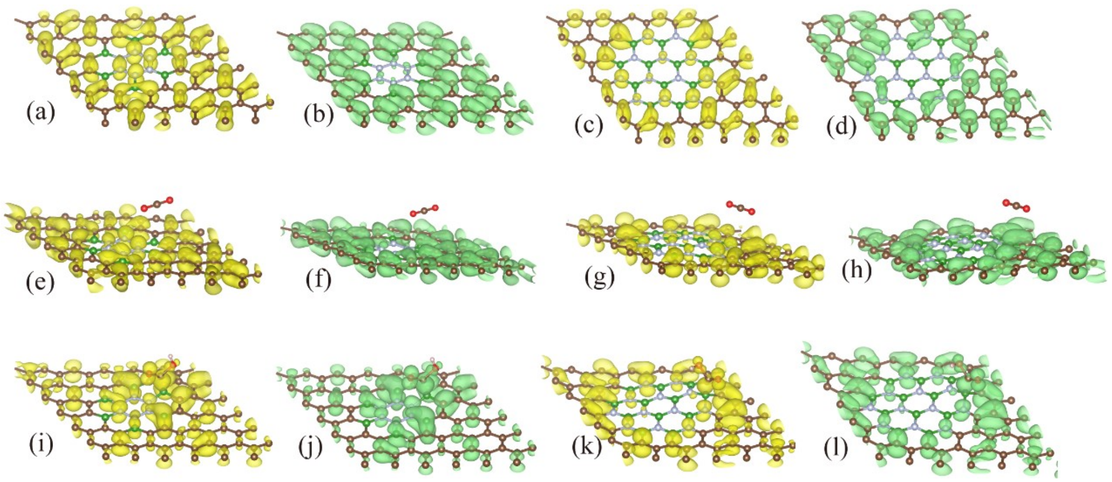

Figure S14. Charge density distributions of the VBM (yellow) and CBM (green) for (a, b) pristine 66Gr-6BN, (c, d) pristine 66Gr-3BN2-7ring, (e, f) $^*CO_2$-adsorbed 66Gr-6BN, (g, h) $^*CO_2$-adsorbed 66Gr-3BN2-7ring, (i, j) *COOH-adsorbed 66Gr-6BN, and (k, l) *COOH-adsorbed 66Gr-3BN2-7ring.

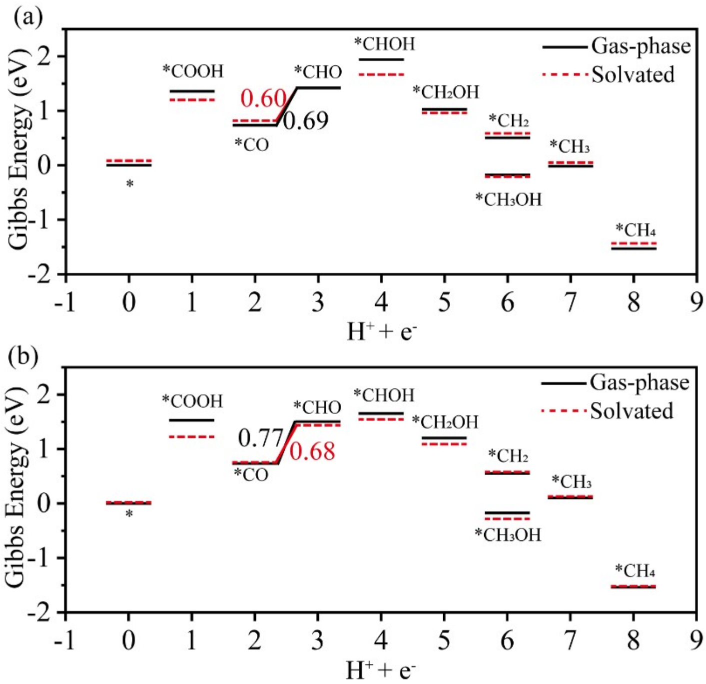

Figure S15. CO_2RR free energy profiles of (a) 66Gr-6BN and (b) 66Gr-3BN2-7ring calculated in the gas phase and with VASPsol correction.

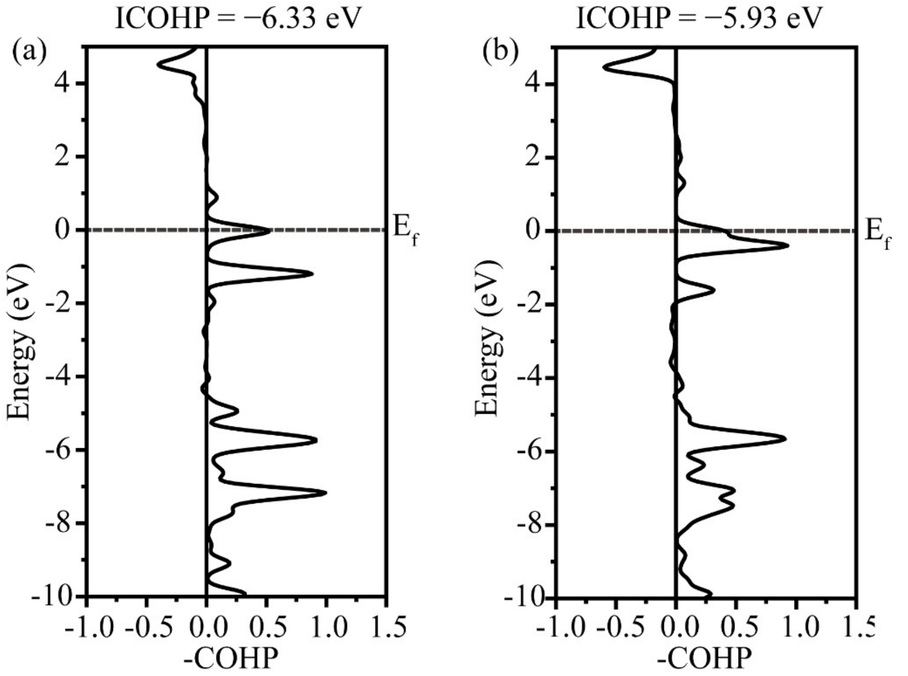

Figure S16. Crystal orbital Hamilton population (COHP) curves of the active-site B–C bond formed in the CHO state on (a) 66Gr-6BN and (b) 66Gr-3BN2-7ring.

Table S4. Rate-determining step (RDS), barrier height, thermodynamic driving force, and catalytic selectivity for CO_2 reduction on representative metal-free 2D photocatalysts,[3] compared with the present structures.

Photocatalyst	RDS	Barrier (eV)	Driving force (V)	Selectivity	Ref.
g-C_3N_4	*HCHO → *CH_3O	1.43	0.67	CH_3OH dominant with minor HCOOH	88
S-doped g-C_3N_4	*CO_2 → *COOH	1.15	0.73	CH_3OH dominant with minor HCOOH; HER competitive (ΔG(*H) = −0.08 eV)	88
h-BN	*CO_2 →	2.33 (CO); 2.19	N/A	Based on barrier	89

Photocatalyst	RDS	Barrier (eV)	Driving force (V)	Selectivity	Ref.
	*COOH	(HCOOH); 2.33 (CH_3OH); 2.33 (CH_4)		heights: HCOOH > CO > CH_4 > CH_3OH	
O-doped h-BN	*COOH → *CO	1.95 (CO); 1.92 (HCOOH); 2.13 (CH_3OH, desorption); 2.03 (CH_4, desorption)	N/A	Based on barrier heights: HCOOH > CO > CH_4 > CH_3OH	89
CTF-1	*CO_2 → *COOH	1.99	0.79	CH_4 56.4%	90
CTFB10	*COOH → *CO	1.21	0.86	CH_4 90.3%	90
TFPT-TMT-COF	*CO_2 → *COOH	1.41	N/A	CO dominant with minor CH_4	S3
66Gr-6BN (this work)	*CO → *CHO	GS: 1.36 (vac) / 1.11 (sol); ES: 0.69 (vac) / 0.60 (sol)	0.69 (CO); 0.84 (CH_3OH); 0.98 (CH_4)	CO_2RR favored over HER ($\Delta G(*H)$ = 1.22 eV); Based on barrier heights: CO > $CH_4 \approx CH_3OH$	—
66Gr-3BN2-7ring (this work)	*CO → *CHO	GS: 1.53 (vac) / 1.21 (sol); ES: 0.77 (vac) / 0.68 (sol)	1.27 (CO); 1.42 (CH_3OH); 1.56	CO_2RR favored over HER ($\Delta G(*H)$ = 1.00 eV);	—

Photocatalyst	RDS	Barrier (eV)	Driving force (V)	Selectivity	Ref.
			(CH_4)	Based on barrier heights: CO > CH_4≈CH_3OH	

Footnote: Method: g-C_3N_4, S-doped g-C_3N_4, h-BN, and O-doped h-BN use DFT-PBE+D2; CTF-1, CTFB10, and TFPT-TMT-COF use DFT-PBE; the present structures use DFT-PBE+D3 for ground-state (GS) calculations and the combined GW-BSE plus excited-state framework described in Section 2 for excited-state (ES) barriers. GS values enable direct comparison with the literature entries.

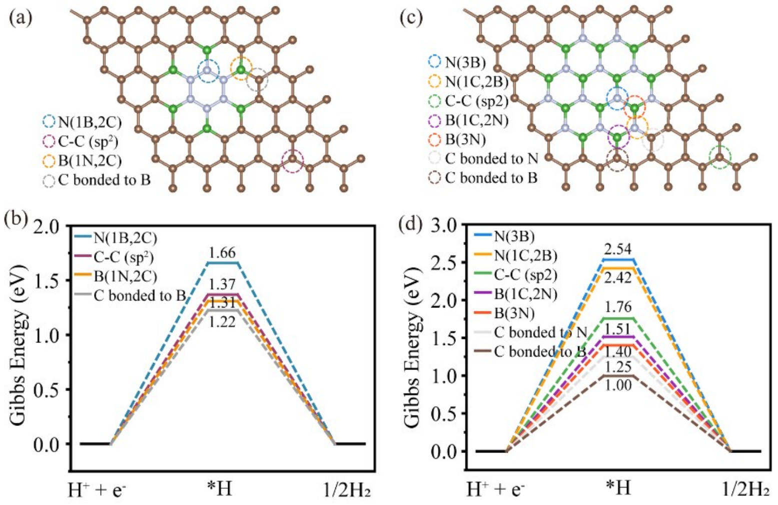

Figure S17. Site-dependent H* formation free energies on (a, b) 66Gr-6BN and (c, d) 66Gr-3BN2-7ring.

References

1. Ola, O.; Maroto-Valer, M. M., Review of Material Design and Reactor Engineering on TiO_2 Photocatalysis for CO_2 Reduction. *J. Photochem. Photobiol., C* 2015, **24**, 16-42.

2. Hu, Z.; Guo, W., Fibrous Phase Red Phosphorene as a New Photocatalyst for Carbon Dioxide Reduction and Hydrogen Evolution. *Small* 2021, **17**, 2008004.

3. Xie, F.; Bie, C.; Sun, J.; Zhang, Z.; Zhu, B., A DFT Study on Pt Single Atom Loaded

COF for Efficient Photocatalytic CO_2 Reduction. *J. Mater. Sci. Technol.* 2024, **170**, 87-94.